

The Effect of Carbon Deposition on Accelerator Grid Wear Rates in Ion Engine Ground Testing*

J. E. Polk, O. Duchemin, C.-S. Ho, B. E. Koel

Abstract

Long duration ion engine testing on the ground inevitably results in the deposition of foreign material, typically carbon, sputtered from the beam target on the thruster. The molybdenum accelerator grid is therefore subject to simultaneous deposition of carbon and sputtering by xenon ions. A major concern in ground testing ion thrusters is that a sub-monolayer coverage of carbon in the areas of net erosion artificially reduces the erosion rate compared to that in space. This paper discusses a surface kinetics model of sputtering for a molybdenum surface subject to a flux of carbon atoms and xenon ions. The model yields the equilibrium surface coverage of carbon and the reduction in molybdenum sputter yield as a function of carbon flux and xenon ion current density and energy. The paper also presents measurements of the cross-sections for ion-induced desorption of carbon from molybdenum, a critical parameter in the model.

Introduction

Xenon ion propulsion is finally entering an age of application in NASA's planetary program. A xenon ion primary propulsion system is one of the key technologies currently being demonstrated on Deep Space 1 (DS1), the first of the New Millennium missions [?]. The single 30 cm ion thruster on DS1 propelled it to an encounter with the asteroid Braille in July, 1999

and is now being used to provide the ΔV for a flyby of the comet Borrelly in 2001. It will deliver a total ΔV of 4.5 km/s to the 486 kg spacecraft during this mission while consuming less than 81 kg of xenon propellant. With this successful demonstration, ion propulsion is now being considered for a broad range of future planetary missions, including the Comet Nucleus Sample Return mission [?], Europa Lander, Neptune Orbiter, Saturn Ring Explorer, Titan Explorer, Venus Surface Sample Return and Mars Sample Return missions [?]. The high specific impulse capability of ion thrusters makes it possible to perform these demanding outer planet and sample return missions using smaller, less expensive launch vehicles and often with shorter trip times. However, the low thrust levels that ion engines provide necessitate extremely long burn times, typically thousands to tens of thousands of hours per engine.

Demonstrating adequate engine life and reliability was a primary roadblock to applications of ion propulsion. This issue was addressed in the NASA Solar Electric Propulsion (SEP) Technology Application Readiness (NSTAR) program through a combination of ground testing and analysis. This program included four major long duration tests to identify unexpected failure modes, characterize the parameters which drive known failure mechanisms and determine the effect of engine wear on performance. In the first test, 2000 hours of operation at the 2.3 kW full power point, several potential failure mechanisms were identified and studied in subsequent shorter duration development tests [?]. The effectiveness of design changes in essentially eliminating these failure modes was then validated in a 1000 hour wear test at full power [?], preparatory to starting an endurance test for the full 8000 hour design life. In this Life Demonstration Test (LDT), a total of 8192 hours of operation were achieved at the 2.3 kW full

*Copyright 2000 by the American Institute of Aeronautics and Astronautics, Inc. The U.S. Government has a royalty-free license to exercise all rights under the copyright claimed herein for governmental purposes. All other rights are reserved by the copyright owner.

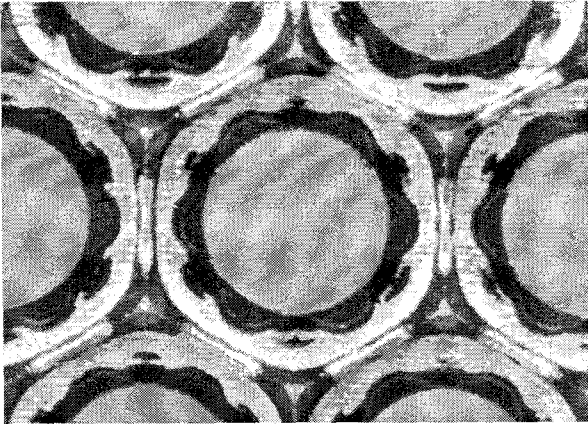


Figure 1: Sputter erosion and carbon deposition observed on the downstream face of the accelerator grid in the NSTAR Life Demonstration Test.

power point before it was voluntarily terminated [?]. A total of 88 kg of xenon propellant was processed, producing a total impulse of 2.73×10^6 Ns. In an ongoing test of the DS1 flight spare ion engine, a total of over 11500 hours of operation at power levels ranging from 1.5 to 2.3 kW have been accumulated and over 100 kg of xenon have been processed [?]. The objective of this test is to demonstrate at least 125 kg of xenon throughput over a range of engine power levels.

One potential failure mode that has been studied in these tests is structural failure of the accelerator grid due to erosion from charge exchange ions [?]. Slow ions are created in the interelectrode gap or downstream of the accelerator grid in charge exchange collisions between beam ions and neutral atoms. Some of these charge exchange ions are accelerated toward the negative accelerator grid and strike the walls of the grid apertures or the downstream face of the webbing between holes. The potential structure formed downstream of the grid by the apertures and the ion beamlets causes the charge exchange ions to be focussed into the center of the webbing between holes. This creates the 'pits and grooves' erosion pattern shown in Fig. (1). The highest ion impingement current density on the downstream face occurs between any three holes, producing a pit. The pits are con-

nected by shallower channels between two adjacent holes. Erosion caused by ions striking the aperture walls causes the holes to enlarge. Eventually, the pits and grooves will penetrate the grid or the hole diameter will grow until it meets the pits and grooves, causing structural failure of the accelerator grid. Hole enlargement may also lead to electron backstreaming, another potential failure mode.

The photograph in Fig. (1) also shows carbon deposits on the downstream face of the accelerator grid. This is most obvious in a dark ring around the apertures. In ground tests, the ion beam from the engine strikes a beam target at the rear of the vacuum chamber. In the 1000 hour test, the 8192 hour LDT and the current test of the flight spare engine the beam target was formed from graphite panels. Graphite was chosen to minimize the amount of material sputtered from the beam target, but carbon atoms are eroded from the panels and some of that backscattered carbon is deposited on the engine. The concern addressed in this paper is that the carbon deposits might form a protective coating that artificially reduces the sputter erosion rate of the molybdenum accelerator grid. This concern was motivated by the fact that bulk carbon has a much lower sputter yield than bulk molybdenum, as shown in Fig. (2). Fortunately, we have found that the sputter yield of carbon adsorbed on molybdenum is much higher than that of bulk carbon, so it does not tend to accumulate in regions subject to sufficiently high ion impingement currents. This is suggested qualitatively by the image in Fig. (1), where there does not appear to be bulk carbon deposition in the pits and grooves erosion pattern. The distribution of erosion and deposition observed experimentally on the grids is discussed in more detail in the next section. In the following section a model of the surface kinetics is used to show that submonolayer coverage of carbon can artificially reduce the molybdenum wear rates. Because it is difficult to determine experimentally if submonolayer levels of contamination are present on the grids, further analysis is used to assess the impact of carbon deposition on ion engine ground testing. The critical parameter in the model is the sputter yield (or cross section) for ion-induced desorption of carbon adsorbates from molybdenum substrates. These cross-sections were measured directly and compared with models of ion-induced desorption to determine

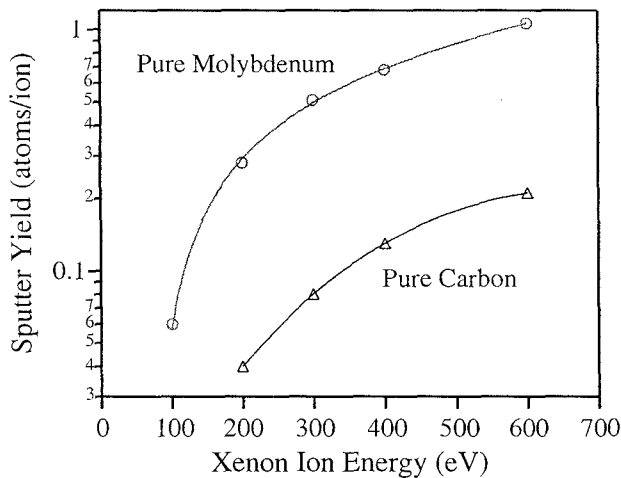


Figure 2: Sputter yields for bulk molybdenum and carbon.

the sputter yield for carbon deposited on molybdenum. These results are applied in the final section to show that backspattered carbon has little effect on ion engine wear rates.

Experimental Characterization of the Deposition and Wear Patterns

The distribution of carbon deposits on the accelerator grid after 8192 hours of operation in the LDT is shown in the optical photographs in Fig. (3) and in the scanning electron microscope (SEM) images in Fig. (4). The SEM images were obtained with backscattered electrons, so they show a sharp contrast between elements. In these photos the white regions are predominantly molybdenum while the black areas are carbon. Net deposition of carbon with no evidence of grid erosion occurred outside a radius of about 11 cm on the grid. Inside this radius the carbon deposits appear to be confined to rings around the individual apertures. The structure of the deposition pattern apparently reflects the distribution of impingement current in the pits and grooves pattern. Net erosion in the pits and grooves pattern is visible on the webbing. The carbon deposition rate was monitored continuously during the test with two quartz crystal microbalances (QCM's) mounted near the engine in the plane of the grids. The deposition rate,

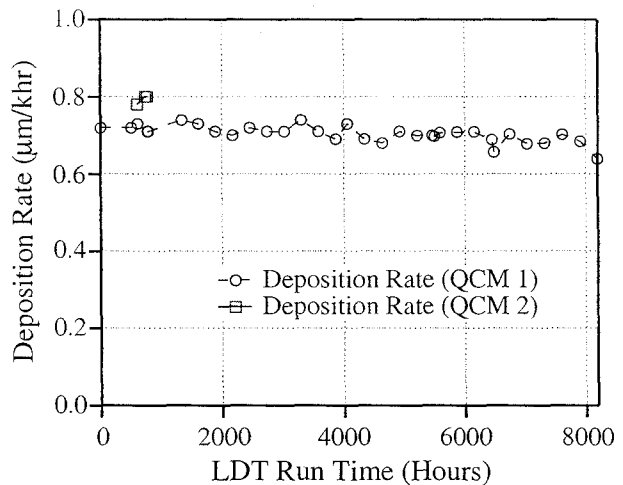


Figure 5: Carbon deposition rate measured during the engine wear test.

plotted in Fig. (5), was nearly constant and equal to 0.7–0.8 $\mu\text{m}/\text{chr}$. Post-test analyses of samples from the QCM's showed dense films with a thickness of 6.0–7.0 μm , which corresponds to a rate of 0.73–0.85 $\mu\text{m}/\text{chr}$. Figure (6) shows an example of a sample from one of the QCM's. Carbon film samples from the downstream face of the grid, such as that shown in Fig. (7), appeared to be more porous and ranged in thickness up to 10 μm . These deposition rates correspond to a carbon flux to the grid plane γ_C of 2.19×10^{12} atoms/ cm^2s .

Mass loss in the three primary erosion sites (hole walls, pits and grooves) was characterized extensively during and after the test. The evolution of the pits and grooves pattern was monitored in situ during the test using a laser profilometer. The grid was sectioned after the test and the geometry of the erosion patterns was further characterized in SEM measurements. In addition, the hole diameters were measured after the test using precision ground pins. These results are reported in [?], and were used to estimate the radial distributions of mass loss per unit grid area plotted in Fig. (8). The highest mass loss rate occurred on the walls of the apertures. The hole wall erosion peaks on the centerline and no wear is visible outside a radius of 11 cm. Integrating this distribution over the

Figure 3: Optical photographs showing the deposition and erosion patterns.

Figure 4: SEM images showing the deposition and erosion patterns. White areas are predominantly molybdenum and black regions are carbon deposits.

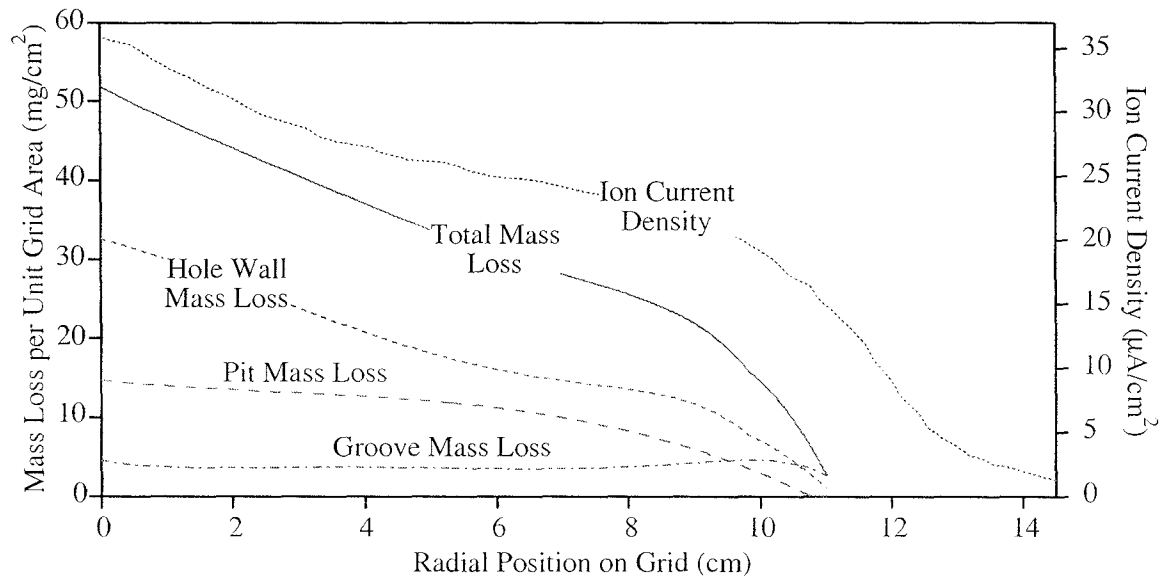


Figure 8: Radial distribution of mass loss and ion impingement current density.



Figure 6: Carbon films removed from the QCM after the wear test.

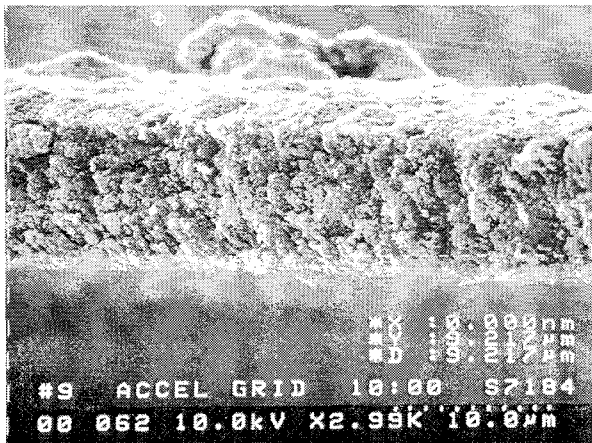


Figure 7: Carbon films removed from the accelerator grid after the wear test.

grid yields a total mass loss from the hole walls of 5.2 g. The distribution of mass loss in the holes can be characterized by a flatness parameter, defined as the ratio of the mass loss per unit area averaged over the whole active area of the grid to the peak mass loss per unit area in the center. These data yield a flatness parameter of 0.251, which shows that it is strongly peaked. The pit mass loss distribution also peaks on the centerline and drops to zero at about 11 cm. The integrated mass loss is 3.0 g and the calculated flatness parameter for this distribution is 0.320. The groove mass loss per unit area is nearly constant with radius. The depth of the groove decreases toward the periphery of the grid, but the length increases as the pit diameters get smaller at larger radial positions. These two effects tend to compensate, yielding a relatively constant mass loss in the grooves between pits. The total mass loss in the grooves is 1.5 g, and the distribution has a flatness parameter of 0.514. The total mass loss distribution is the sum of the losses from the three sites, and yields a total mass loss of 9.7 g. This agrees with the measured total mass loss of 10.81 g to within about 10 percent. The overall flatness parameter for grid mass loss is 0.293. The flatness parameters are much smaller than observed in previous tests [?]. This is a result of the complete lack of erosion at the grid periphery where the net carbon deposition was observed—there is no mass loss over a substantial fraction of the active grid area.

Figure (8) also displays an estimate for the radial distribution of the impingement current density in the pits and grooves pattern. The beam current density was measured directly by sweeping a Faraday probe across the beam at a distance of approximately 2.5 cm from the plane of the grids. Assuming a uniform flow of neutral atoms from the grids, the charge exchange ion production rate downstream of the optics is proportional to the beam current density. If the charge exchange ions are not created too far downstream, they will tend to strike the grid at radial positions close to those where they were created. The radial distribution of charge exchange ion current density will therefore follow that of the beam current density. With these assumptions, the average ion impingement current density in the pits and grooves pattern can be estimated using the expression

$$\overline{j_a} = \frac{\beta}{(1 - \phi_a)\alpha} \left(\frac{j_a}{j_b} \right) j_b, \quad (1)$$

where β is the fraction of the total impingement current $J_a = 6.78$ mA that strikes the downstream face of the grid, $\phi_a = 0.24$ is the physical open area fraction of the grid, α is the fraction of the webbing area covered by the pits and grooves erosion pattern, $J_b = 1.76$ A is the total beam current and j_b is the beam current density as a function of radius. The parameter β was assigned a value of 0.46 based on the ratio of the mass loss in the pits and grooves to the total mass loss. The eroded area fraction α was about 0.41, based on the measured widths of the grooves on the grid. This method of estimating the distribution parameters from measured erosion patterns is somewhat suspect, because the erosion patterns may be influenced by the carbon deposition. This approach is justified by the conclusions of the analysis presented below. The pit depths are approximately four times higher than the average depth in the pits and grooves pattern, suggesting that the ion current density in the pits is about four times higher than the average shown in the plot. Similarly, the groove current density is slightly less than the average plotted. The plot shows that the mass loss distribution tends to follow the impingement current density distribution, but drops to zero at a radial location where the average ion current density is equal to about $17 \mu\text{A}/\text{cm}^2$.

These results suggest that the net carbon deposition rate is very low in regions where the ion current density is sufficiently high. This concept is explored quantitatively in the next section.

A Model of the Effect of Carbon Deposition on Molybdenum Erosion Rates

Three species participate in the kinetics on the surface and subsurface of the grids—molybdenum atoms in the substrate, adsorbed carbon atoms and xenon ions. Three collisional processes which are shown schematically in Fig. (9) determine the sputter rates of molybdenum and carbon atoms. In Interaction I, a bombarding xenon ion strikes a carbon adatom. This interaction can reduce the molybdenum sputter yield because the incident ion will lose up to 31 percent of its initial energy in the collision. This collision may result in sputtering the carbon atom if it has sufficient energy after interacting with the molybdenum substrate to overcome the binding energy U_c . The probability of this interaction is proportional to the carbon surface coverage $\theta_C = N_C/N_0$,

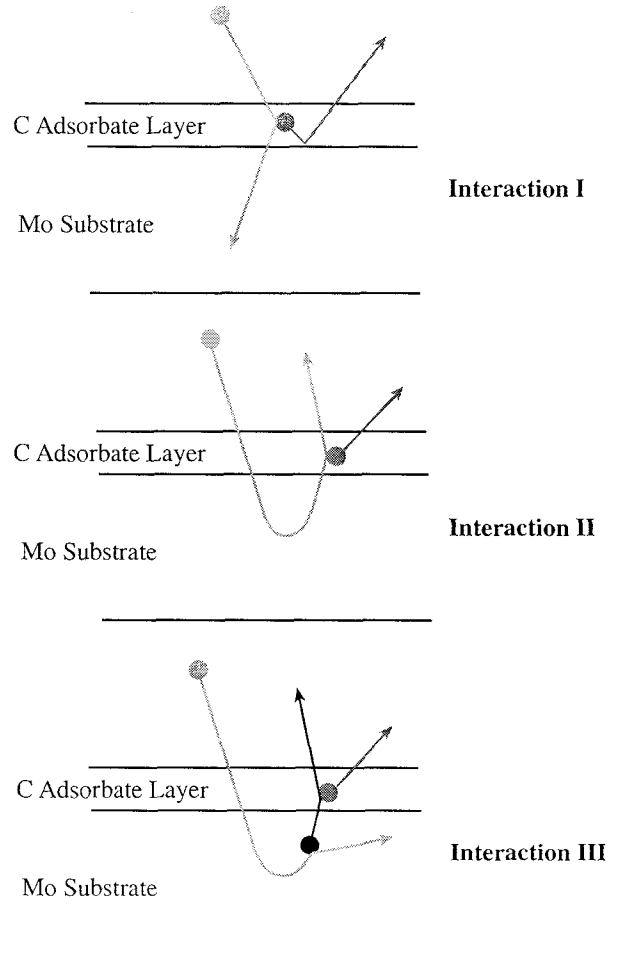


Figure 9: Collisional processes which determine the effect of surface carbon atoms on the molybdenum sputter yield.

where N_C is the surface density of carbon adatoms and $N_0 = 1.2 \times 10^{15}/\text{cm}^2$ is the density of available adsorption sites.

Interaction II occurs when a xenon ion is reflected off of the molybdenum substrate and collides with a carbon adatom. This process does not affect the molybdenum sputter yield because it occurs after the ion has left the surface, but may result in carbon sputtering if sufficient energy is transferred to overcome the surface binding energy. The probability of Interaction II is also proportional to the carbon surface coverage.

Interaction III occurs when a molybdenum atom set in motion by the collision cascade from an incoming xenon ion strikes a carbon surface atom. This process may reduce the net molybdenum sputter yield because the Mo atom loses up to 40 percent of its energy in the interaction and may result in carbon sputtering if the transferred energy exceeds the binding energy. The probability of a type III interaction is also proportional to the carbon surface coverage.

If we conservatively assume that molybdenum sputtering does not occur if interaction I or III occur, then the net molybdenum sputter yield is

$$Y_{Mo}^{net} = Y_{Mo}(1 - \theta_C). \quad (2)$$

No molybdenum sputtering occurs if the carbon surface coverage is unity, only net carbon deposition. If the surface coverage is zero, there is no effect on the molybdenum sputter yield. The areas which clearly have net erosion are only affected by submonolayer carbon films. The rate-of-change of the carbon surface coverage is determined by the carbon flux γ_C and the ion-induced desorption rate, or rate at which carbon adatoms are sputtered by xenon ions,

$$\frac{dN_C}{dt} = \gamma_C - \left(\frac{j_a Y_{C-Mo}}{e N_0} \right) N_C. \quad (3)$$

In this expression j_a is the ion impingement current density, e is the electron charge and Y_{C-Mo} is the sputter yield for C adatoms on Mo. The equilibrium surface coverage is

$$\theta_C = \frac{e \gamma_C}{j_a Y_{C-Mo}}. \quad (4)$$

The reduction in the Mo sputtering rate is given by

$$\frac{Y_{Mo}^{net}}{Y_{Mo}} = 1 - \frac{e \gamma_C}{j_a Y_{Mo}} \left(\frac{Y_{Mo}}{Y_{C-Mo}} \right). \quad (5)$$

This confirms our conclusions based on the experimental erosion and deposition patterns; the pattern is unaffected if there is very little carbon deposition and the ability to maintain a clean surface depends on the relative sputter yields and the ion impingement current density compared to the carbon flux. Unfortunately, none of the experimental methods employed in the grid examinations have sufficient sensitivity to detect carbon contaminants at the submonolayer level. In addition, clean metal surfaces are very rapidly contaminated with thin carbon films after exposure to air, so it is impossible to determine experimentally now if the eroded areas were free of carbon contaminants during the test. Instead, we must rely on the use of this model and estimates of the input parameters to determine if the erosion rates were affected by the backspattered carbon. Estimates of γ_C and j_a from the test results were presented in the previous section and Fig. (2) gives the value of Y_{Mo} . The sputter yield for carbon deposited on molybdenum is discussed in the next section.

Ion-Induced Desorption of Carbon Adatoms from Molybdenum

The measurement of the ion-induced desorption cross-sections of carbon on molybdenum was performed in a static experiment, i.e. with no flux of incoming carbon atoms during the ion bombardment. In-situ, controlled deposition of carbon in the monolayer-range was achieved on an atomically clean Mo(100) single crystal surface before bombarding the sample with an energetic ion beam. Appropriate surface diagnostics were then used to determine carbon surface coverage as a function of bombarding ion fluence.

Among the variety of popular quantitative surface analysis techniques, Ion Scattering Spectroscopy (ISS) has the unique particularity of being extremely sensitive to the first atomic layer [?] and was therefore chosen to monitor the carbon coverage on the molybdenum substrate. As shown in Fig. (10), the incoming ions are scattered by the surface atoms and collected in an electrostatic energy analyzer. The scattering angle θ being fixed by the relative alignment between the ion source and the energy analyzer, the ratio between the energy of the scattered ions and the energy of the incident ions is then only a function of the mass ratio between the incoming ions and the scattering

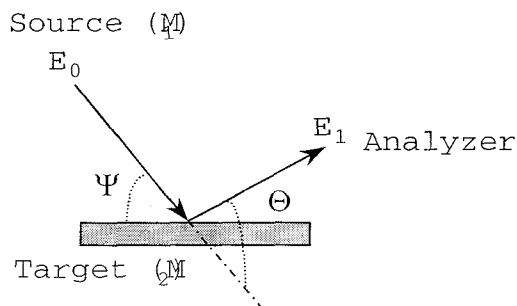


Figure 10: Collisional processes which determine the effect of surface carbon atoms on the molybdenum sputter yield.

center at the surface. The peaks in collected current over the energy range scanned by the analyzer correspond to the different atomic masses of atoms present in the top monolayer.

Since this study was interested in the desorption induced by normally-incident ions, the incidence angle ψ had to be zero degrees. This condition of normal incidence could not allow operation of ISS in forward-scattering mode, and the heavier atomic mass of xenon compared to both carbon and molybdenum also made back-scattering ISS impossible. It was therefore necessary to use a mixture of a lighter gas argon and xenon to allow simultaneous desorption by xenon ions and back-scattering ISS using the argon beam.

The experiments were carried out in a Ultra High Vacuum (UHV) system at the Department of Chemistry, University of Southern California. The base pressure was $1\text{E-}8$ Pa ($1\text{E-}10$ Torr) and the system, represented in Figures (??) and (??), contained a differentially pumped Colutron 10kV ion gun, a Perkin-Elmer Model 10-360 Spherical Capacitor Analyzer (SCA) at a fixed 144-deg. scattering angle, usable for ISS and X-ray Photoelectron Spectroscopy (XPS). Other capabilities included in the chamber are Auger Electron Spectroscopy (AES) and Low Energy Electron Diffraction (LEED).

The Mo(100) sample (Atomeergic Chemetals Corp.) was a 10-mm diameter x 1.5-mm thick single crystal cut within ± 0.5 deg. The crystal was held on the sample holder between two 0.4-mm tungsten wires used to resistively heat the sample. Temperatures were measured by a thermocouple junction spot-welded to the edge of the crystal.

At the indicated base pressure, the monolayer formation time for oxygen appeared to be of the order of an hour, while it is expected to be 30 hours for carbon containing species [?]. Overnight, surface layers built up to yield an Auger Peak to Peak Height (APPH) ratio of typically 40day.

To perform the initial cleaning of the surface, the sample was first submitted to an oxygen treatment at an oxygen partial pressure of $1.3\text{E-}5$ Pa ($1\text{E-}7$ Torr) at 800 K, for 2 minutes. The oxygen treatment removed the carbon surface layer by forming CO, which then evaporated. A new AES analysis typically yielded an APPH ratio close to 0 and 100 oxygen. The APPH ratio at this point was expected to be of about 20 new

Figure 11: Ultra high vacuum facility used to measure the ion-induced desorption cross sections.

Figure 12: Ultra high vacuum facility used to measure the ion-induced desorption cross sections.

traces of carbon at the surface was due to carbon diffusion from the bulk during the brief annealing. If more carbon was present, the cycle was repeated in order to lower the bulk concentration of carbon.

A controlled carbon monolayer was then grown on the sample surface by dosing 20 Langmuirs ($1\text{E-}7$ Torr x 200 sec.) of ethylene (C_2H_4) at the sample surface at 850 K to thermally crack the hydrocarbon and desorb hydrogen from the surface, leaving behind carbon adatoms [?, ?]. This method has been reported to deposit a saturated p(1x1) carbon monolayer on the molybdenum surface for a C/Mo APPH ratio of 0.36 ± 0.01 [?]. The annealing temperature was a trade-off between a sufficient temperature to carburize the surface while avoiding carbon diffusion into the bulk. The sharp p(1x1) LEED pattern obtained was in accordance with the literature, but the C/Mo APPH ratio was close to 32

When a uniform ion beam with current density j_0 impinges on a sample surface, the decrease dN_a/dt of the surface density of the adsorbate with time is given by [?]

$$-dN_a/dt = j_0 \sigma_D N_a(t) \quad (6)$$

where σ_D is the desorption cross-section. With the assumption that the intensity of the signal of the ion scattering is proportional to the surface density of the scattering centers

$$I_a(t) = C_a N_a(t) \quad (7)$$

where C_a mostly depends on the scattering cross-section and the neutralization probability for the incident ion. The decrease in ISS signal for the adsorbate with increasing ion fluence is therefore described by

$$I_a(t) = C \exp(-\sigma_D j_0 t) \quad (8)$$

where C is a constant. Since argon ions are not backscattered by carbon adatoms however, the rise of the substrate signal can be monitored instead and we have equivalently:

$$I_s(t) = I_s(\infty) + C \exp(-\sigma_D j_0 t) \quad (9)$$

where $I_s(t)$ is the signal intensity for the substrate atoms. By monitoring the rise in the ISS substrate signal with time, or rather ion fluence, it is then a matter of fitting this exponential form to the data

and repeating the experiment for different values of incident ion energy to obtain the energy dependence of the desorption cross sections.

Three data points each were obtained for the desorption of carbon on molybdenum by argon and neon. In both cases, the gas was introduced pure in the ion source. In the case of xenon-ion induced desorption however, and as discussed earlier, a 2/1 mixture of argon and xenon was used. An ExB velocity filter shown in Fig. (13) downstream of the ion optics was used to select the xenon ion beam to desorb the carbon layer, or the argon ion beam to perform the ISS diagnostics at regular time intervals.

The downstream aperture of the ion gun was 2 mm^2 in size, and the beam parameters including focusing were adjusted as to optimize the beam current on a fixed Faraday cup placed downstream of the sample. An important discrepancy, usually a factor of 3 to 5, was found between the beam density as measured by the Faraday cup, and the beam density as inferred by the sample current. This was believed to be caused by a slight misalignment of the Faraday cup and the beam, possibly due to imprecise positioning of the Faraday cup or beam deflection by the ion optics. The beam current density was therefore inferred from the sample current, with the ion gun assumed to generate a well collimated, uniform beam with spot size of 2 mm^2 (1.6-mm diameter). This assumption is supported by the fact that an ion beam of this diameter with a current density of 2 nA/mm^2 , typical in the experiments described here, assumed fully non-neutralized and with an energy of 400 eV (worst case) would have a divergence angle smaller than 0.01 deg.

Another correction was brought to the data acquired for molybdenum to account for the desorption induced by the argon beam during the ISS diagnostics. The argon cross sections were used along with an initial guess of the xenon cross sections to calculate an equivalent xenon ion fluence accumulated on the analysis area by the argon ion beam during the approximately 1-min. long ISS scan. After several iterations a ratio of 7 between the xenon cross sections and the argon cross sections was found to be satisfactorily self-consistent. Due to the usually lower argon current compared to the xenon current, and lower argon cross sections, this correction proved to be rather minor and of the order of a few percent,

Figure 13: Ion source used in the ion-induced desorption experiments.

except on one occasion when the argon current was noticeably larger than the xenon current (correction of 20

The ISS signal used was the integrated area under the molybdenum peak, expressed in relative, arbitrary units and scaled with the sample current to correct for small variations of the incident ion beam current density. Example plots of the ISS signal versus ion fluence along with the corresponding exponential fit are shown in Figures (14) and (15). The experimental cross sections obtained here are summarized in Fig. (16).

The rather large spread in the data has been noted by other authors to be possibly caused by particle prebombardment and changes in surface roughness [?, ?, ?]. In addition, small variations in the level of carburization of the surface could cause an overlayer of carbon adatoms with smaller binding energy to form, possibly changing the measured desorption cross section. It is particularly interesting to notice that in the two cases where consecutive experiments were performed on different regions of the sample without a new surface preparation, the mea-

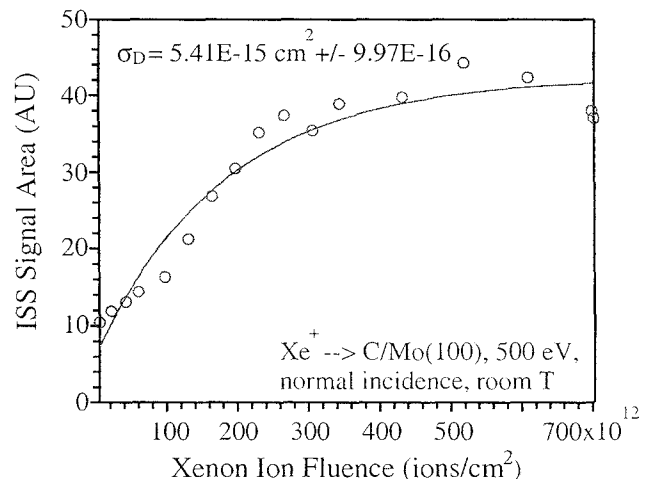


Figure 14: ISS signal for molybdenum measured during bombardment with 500 eV xenon ions.

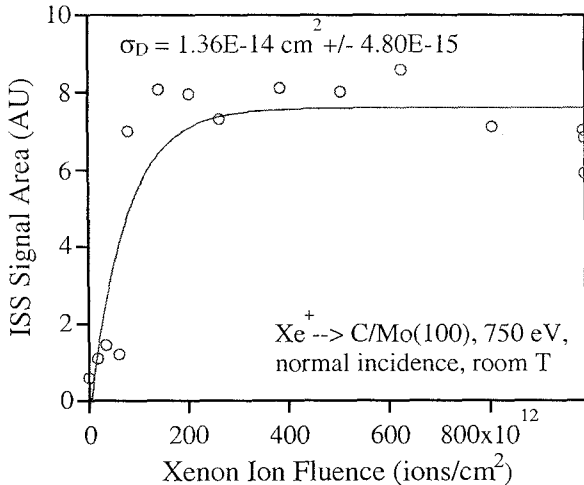


Figure 15: ISS signal for molybdenum measured during bombardment with 750 eV xenon ions.

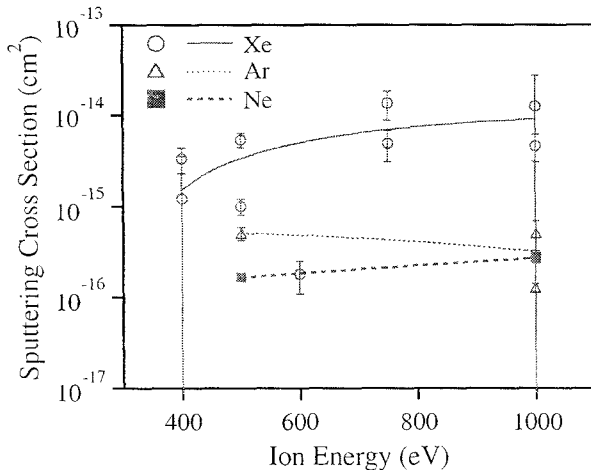


Figure 16: Measured cross sections for ion-induced desorption of carbon from molybdenum.

sured desorption cross sections were remarkably consistent (i.e. xenon cross sections of $1.25\text{E-}14$ at 1 keV and $1.36\text{E-}14$ at 750 eV, and xenon cross sections of $4.61\text{E-}15$ at 1 keV and $5.41\text{E-}15$ at 500 eV). Overall, the data seem to agree in range with the published literature [?] for argon and neon, while it is noticeably higher for xenon, for which few cross sections are available for comparison.

An Assessment of Ground Test Effects on Molybdenum Wear Rates

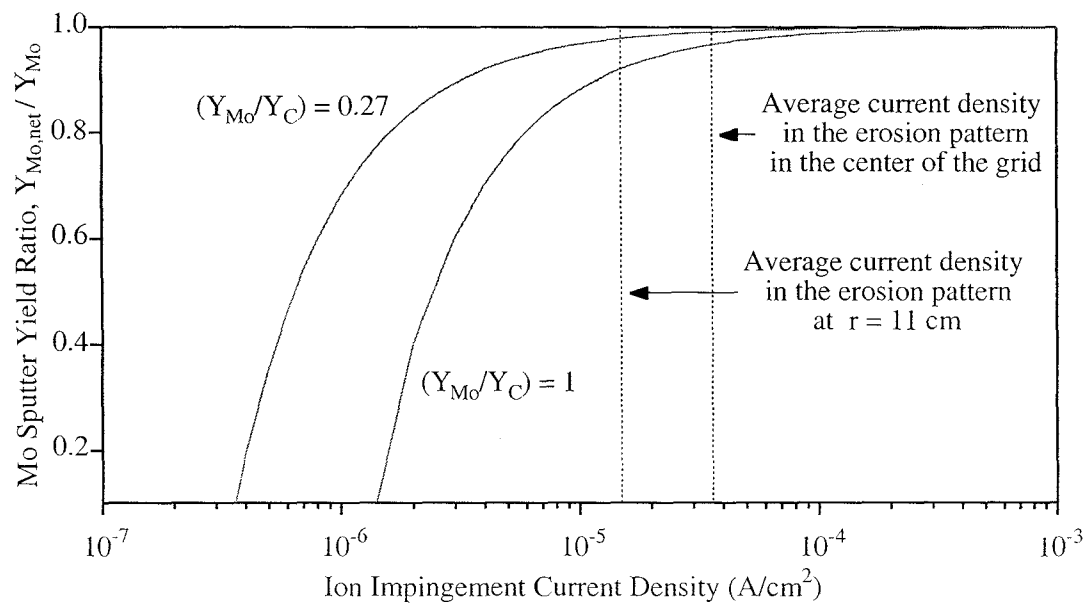
The ion-induced desorption cross-sections presented above can be used with the surface kinetics model to evaluate the reduction in the molybdenum sputter rate as a function of ion impingement current density. The sputter yield for carbon adsorbed on molybdenum is given by

$$Y_{C-Mo} = N_0 \sigma_D \quad (10)$$

The density of surface sites on molybdenum is $1.1 \times 10^{15} \text{ cm}^{-2}$ and the cross section for xenon at relatively low energies is about $1 \times 10^{-15} \text{ cm}^2$, which gives a yield of 1.1. At a xenon ion energy of 200 eV, the corresponding yield for molybdenum sputtering is 0.295, so the ratio Y_{Mo}/Y_{C-Mo} has a value of 0.27. This value and the measured carbon deposition rate were used to calculate the reduction in Mo sputter yield, which is plotted as a function of ion impingement current density in Fig. (17). The average impingement current density in the center of the grid and at a radius of 11 cm (on the boundary between net deposition and net sputtering) is shown as vertical lines on the plot. These data clearly show that the effect of carbon deposition on ion engine grid wear rates is negligible everywhere except where the ion impingement current density is very low. The erosion rates measured in the long duration tests can therefore be used with confidence in predicting engine behavior in space.

Acknowledgements

The research described in this paper was conducted in part at the Jet Propulsion Laboratory, California Institute of Technology, and was sponsored by the National Aeronautics and Space Administration.



[h]

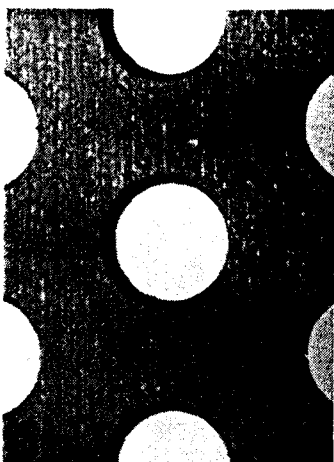
Figure 17: Effect of carbon deposition on molybdenum sputter rates.



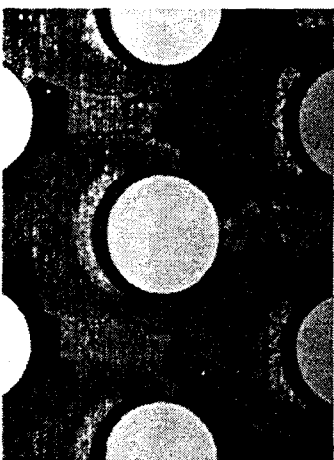
FIG. 3.

Optical Photos of the Deposition Pattern

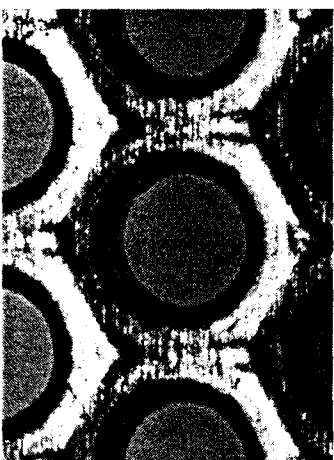
JPL



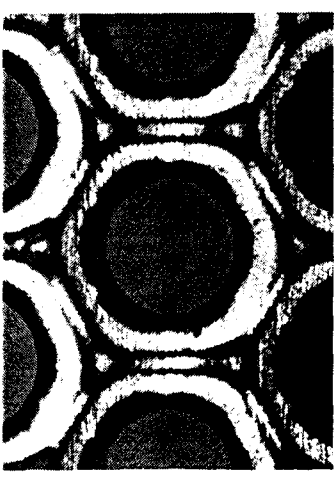
$r = 14 \text{ cm}$



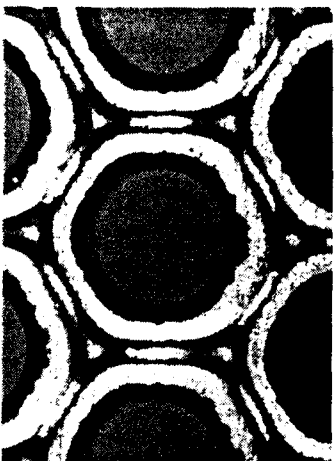
$r = 12 \text{ cm}$



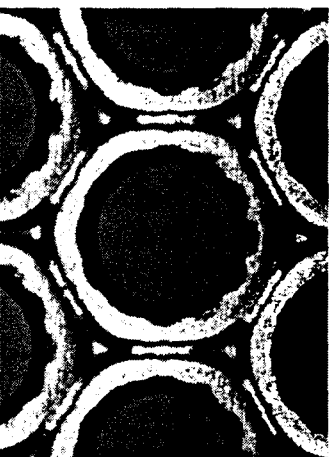
$r = 10 \text{ cm}$



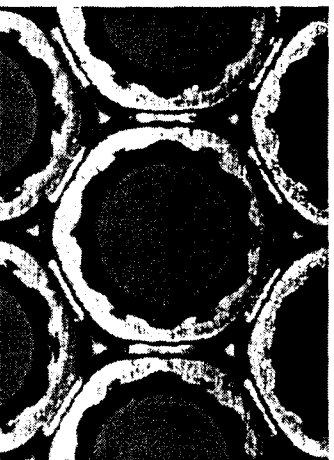
$r = 8 \text{ cm}$



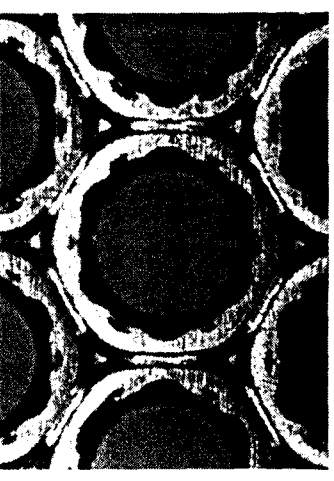
$r = 6 \text{ cm}$



$r = 4 \text{ cm}$



$r = 2 \text{ cm}$



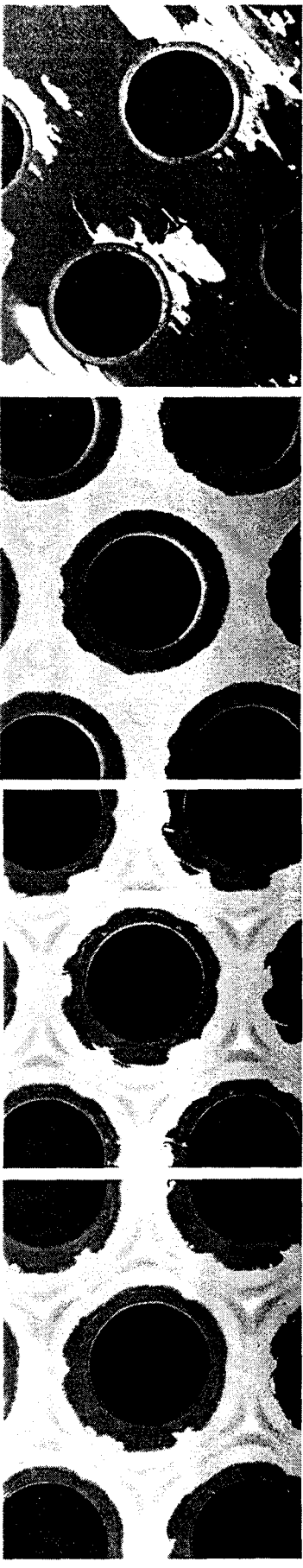
$r = 0 \text{ cm}$



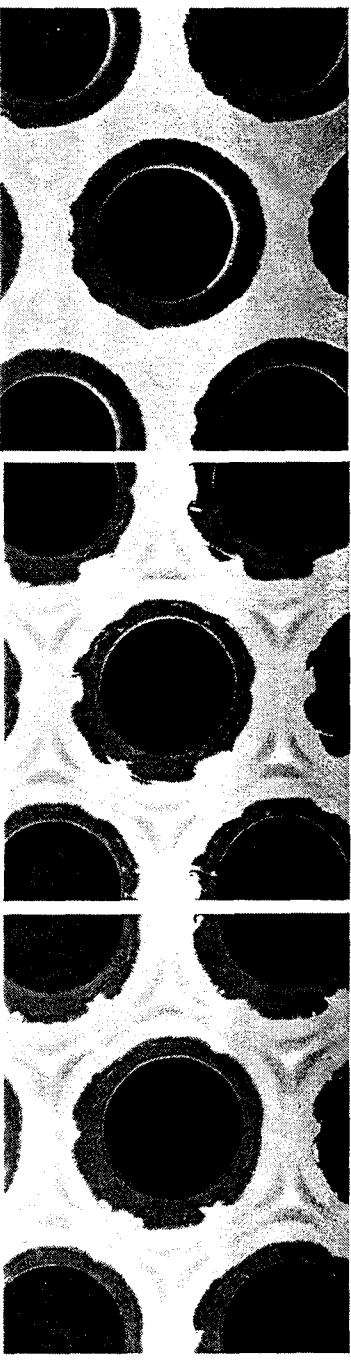
FIG 4,

SEM Photos of the Deposition Pattern (Back-scattered Electrons: White is Mo, Black is C)

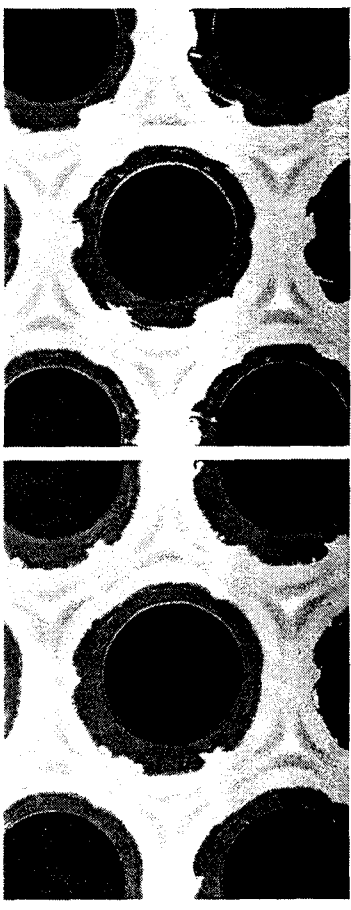
JPL



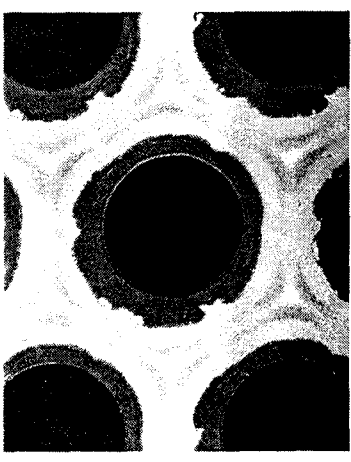
$r = 12.1$ cm



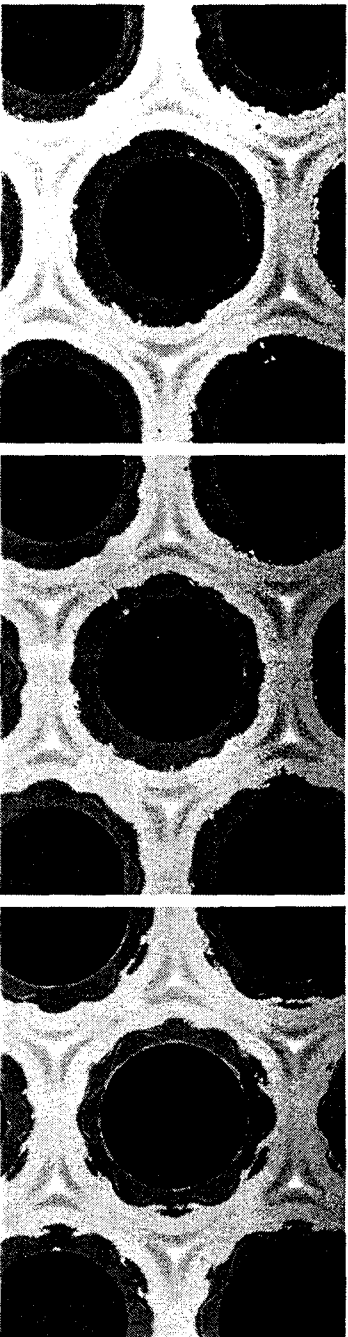
$r = 10.7$ cm



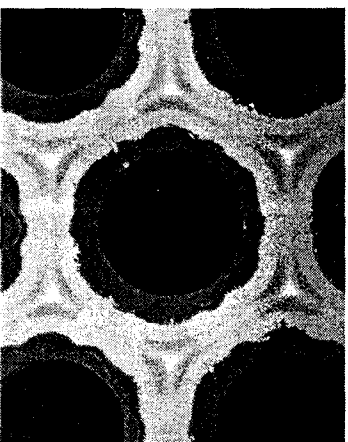
$r = 8.2$ cm



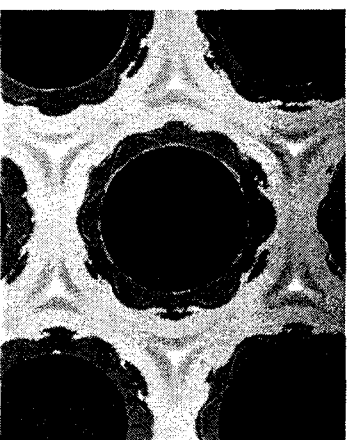
$r = 5.8$ cm



$r = 4.5$ cm



$r = 1.9$ cm



$r = 0.0$ cm

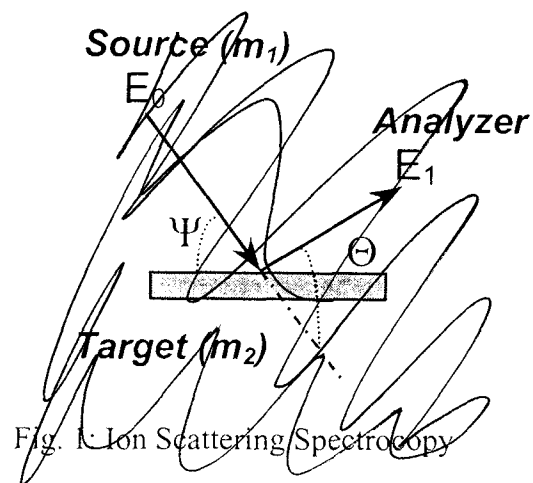


Fig. 1: Ion Scattering Spectroscopy

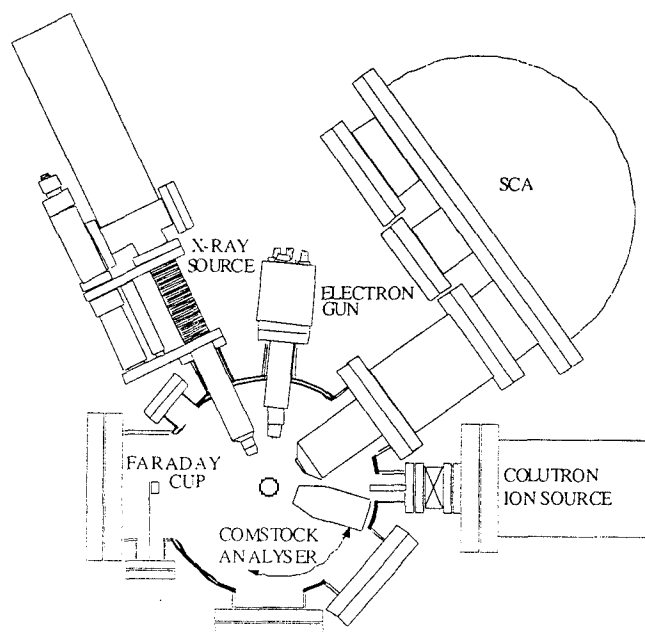
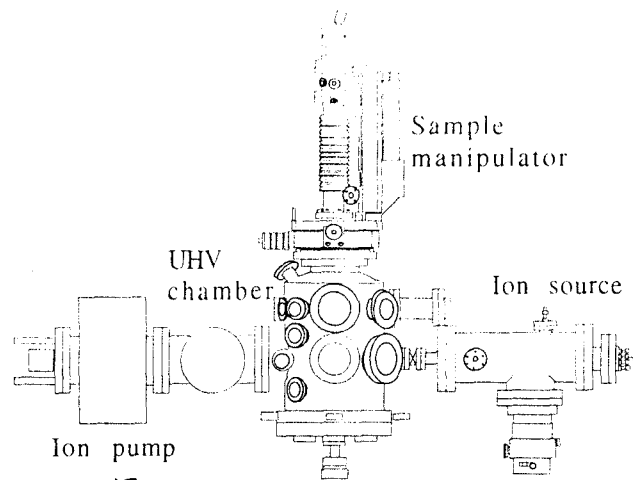


FIG 11

~~Fig 2~~: UHV System (lower level)



12
Fig. 12: UHV system (general view)

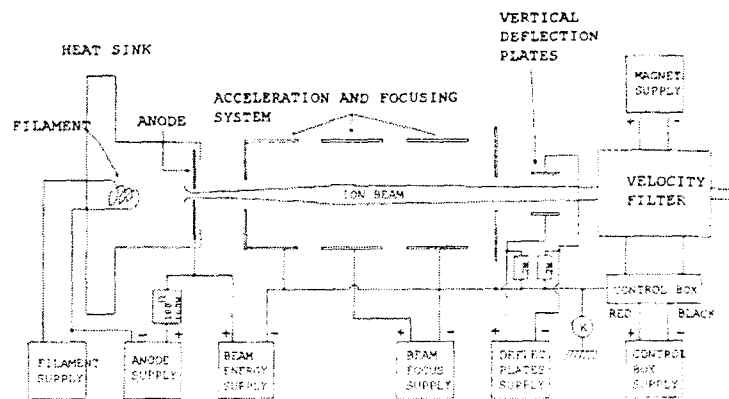


Fig. 13: Colutron Ion Source
13